RESEARCH PAPER

Heat development of the contact area during capacitor discharge welding

Max-Martin Ketzel[1] · Martin Hertel[1] · Jörg Zschetzsche[1] · Uwe Füssel[1]

Abstract

Capacitor discharge welding primarily applies to projection welding. Components with ring projections up to 200 mm diameter can be welded with peak currents up to 1000 kA and welding times less than 10 ms. Weld nuggets are expected to occur, as the CD-Welding belongs to resistance welding. Although the required strength is given, welding nuggets in cross-sections cannot invariably be verified. According to recent researches, joining occurs without a welding nugget, but with metal vaporisation and linked activation of the surfaces. This process is called short-time welding with high thermal current density. The type of the welded joint depends on the heating properties in the weld zone. Different welding energies, electrode forces and welding times result in different welded joints. The process-specific advantages can be taken, and new application areas for CD welding can be developed by knowing the cause-and-effect relationships.

1 Introduction

Capacitor discharge welding (CDW) is one of the oldest welding processes. As early as 1766, the potential of energy stored in a capacitor was recognised for joining [1]. According to [2, 3], it is assigned to pressure welding with current as source of energy. Therefore, CDW belongs to resistance welding processes. It is usually used for projection welding which also belongs to resistance welding processes. Components with ring projections up to a diameter of 200 mm can be welded with peak currents up to 1000 kA and welding times less than 10 ms. There are several advantages of CDW. The energy input per welding is constant and does not depend on the resistance of the joint. Compared with welding with AC or DC sources, the workload of the electrical grid is low due to slow charge of the capacitors within breaks between the welds. Since the welding times are very short

✉ Max-Martin Ketzel
max-martin.ketzel@tu-dresden.de

[1] Institute of Manufacturing Technology, Chair of Joining Technology and Assembly, Technische Universität Dresden, Dresden, Germany

(< 10 ms), there is almost no heat conduction during the welding process. Therefore, heat influence on the surrounding material is very low. That is why CDW is qualified for hardened and tempered gear wheels, material combinations with high CEV values and parts with high surface requirements (for example high-alloy steels without priming paints). [4–6]

As CDW is classified as a resistance welding process, the formation of a weld nugget without expulsions can be expected, as usual with resistance projection welding [7]. Usually, at CDW, there are little expulsions while cross sections do not show weld nuggets but joints without dilutions between the base materials of the joining partners, although the required strength is given. Figure 1 shows a comparison of projection welded nuts with DC welding and CD welding.

The new knowledge of the CDW process, which is called "short time welding with high heat flux density", can explain this behaviour [10]. According to recent researches, joining occurs without a weld nugget but with metal vaporisation and linked activation of the surfaces.
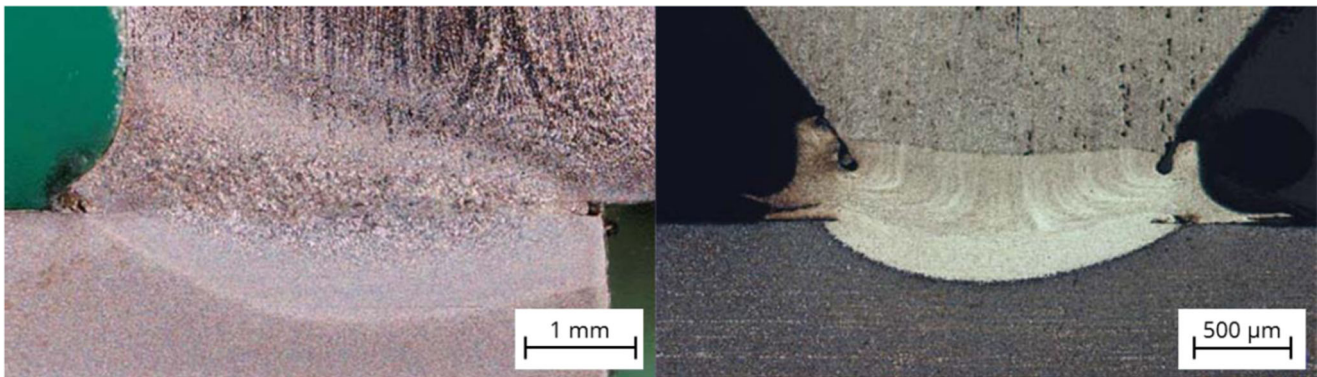
2 Welding experiments and results

There are many possible projection geometries [11–13]. In order to explore process fundamentals, a simple projection geometry (Fig. 2) is used for welding experiments. The

Fig. 1 Left: projection welded nut (19MnB4) to sheet metal (CP800) with DC (I_S = 20 kA, t_S 100 ms) [8]; right: weld specimen with projection (25CrMo4) to sheet metal (42CrMo4) with CDW (4800 Ws) [9]

materials for the specimen are S235JR for the projection geometry and 22MnB5 + AS150 (hot-stamped) with sandblasted surface (sandblasted in a blast cabinet with corundum and handheld gun) for the sheet metal. The chemical compositions of the tested materials are shown in Table 1. The experiments are welded with a CD-welding-machine with the properties:

– Max. loading energy 12,000 Ws
– Max. electrode force 30 kN, servo-electrical actor
– Follow-up mechanism (Nachsetzeinheit) with four belleville springs, c = 3.1 kN/mm
– Transformer ratio a = 20, time to peak current t_p = 1.9 ms, welding time t_h = 4.2 ms

During the experiments, the welding force and the loading energy are changed in order to create a weldability lobe. At first, a high welding force ($\approx$ 18 kN) is chosen. Then specimens are welded with increasing loading energy (starting at 500 Ws in steps of 250 Ws). If there are too much expulsions (subjective assessment) the welding force is reduced (by 2.5 kN in settings, machine does not work correctly, Figure 4 shows measured values) and the loading energy starts again at 500 Ws.

During the experiments, data recording of welding current and electrode voltage with 200 kHz sampling rate are measured. The data of the electrode voltage is corrected computationally from the interference voltage which is induced as a consequence of the great changes in amperage during the welding process [16]. Furthermore, high-speed-recordings with 20,000 fps are taken synchronously to the data recording.

The welds are destructively tested by the chisel test in comprehension to [17]. Therefore, the specimen is mostly stressed with a mechanical strain in normal direction [17]. The result of the chisel test is the type of failure and geometric data of the weld.

There are two possible results of the chisel test at this investigation, a ring weld and a plug failure. Ring welds are characterised by a fracture area in the form of a ring at the edge of the projection. Plug failures occur when the maximum shear stress of the sheet metal material is reached. As the failure plane is bigger at plug failures (approximately plug circumference multiplied with sheet thickness), the loadability is higher at this type of failure. During the welding process, expulsions are subjectively assessed. In order to objectify this assessment, video recordings of the welding experiments are taken (freeze images from the videos are shown in Fig. 3). The expulsions are categorised into four classes: from class 0 (without visible expulsions) to class 3 (high amount of
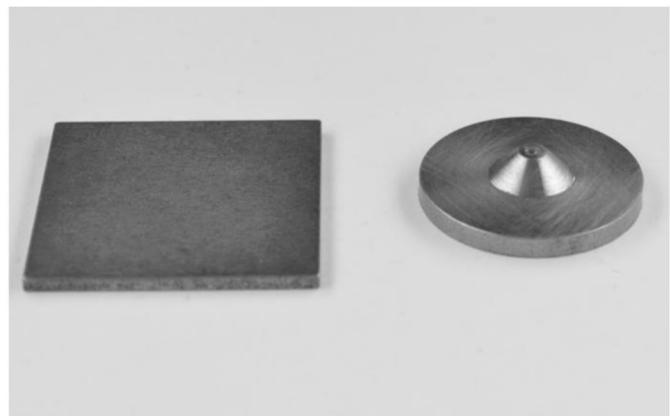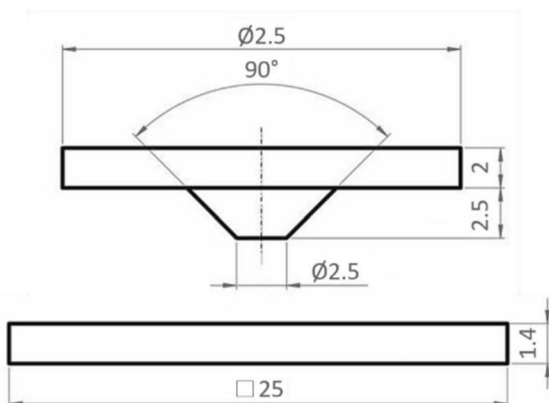
Fig. 2 Left: technical drawing of the single projection and sheet metal; right: turned single projection with laser cut sheet metal

Table 1 Chemical composition of the tested materials [14, 15]

		C	Mn	Si	P	S	Al	Ti	Cr	B	Mo	Cu	Ni
S235JR	Min.	–	–	–	–	–	–	–	–	–	–	–	–
	Max.	0.19	1.5	–	0,045	0,045	–	–	–	–	–	0.6	–
22MnB5	Min.	0.22	1.2	0.2	–	–	0.02	0.02	0.11	0.002	–	–	–
	Max.	0.25	1.4	0.3	0.02	0.005	0.05	0.05	0.2	0.0035	0.1	0.1	0.1

expulsions which partly glow longer than 1 s). Comparing the experiments to these recordings allow a classification for every welding.

The weldability lobe (Fig. 4) shows obvious decreasing loadability (type of fracture) and trend of expulsion with increasing welding force plus increasing loadability and trend of expulsion with increasing loading energy.

In order to understand the physical fundamentals, a simulation model is needed because processes within the joint plane cannot be resolved locally by measuring. The finite-volume-method (FVM) is used for the simulation. The model is created halved and two dimensional as it is usual for rotationally symmetric components. Figure 5 shows the model rotated out. Joule heating, charge conservation, i.e. the current density distribution depending on bulk resistances, contact resistances and temperature-dependent material properties

are implemented. The contact resistance (ECR) is determined by Eq. 1 with the contact pressure P (determined of the measured welding force and the theoretical contact area), the thickness d of a thin, artificial contact layer (commonly set as 0.05 mm), factor K for adjustment in the existence of Al oxide layers (is set to 1.0) and the material- and temperature-dependent parameters σ_S (yield stress of the softer material) plus the electrical resistivity ($\rho_{R1}(T)$ and $\rho_{R2}(T)$) of both materials in contact [18]. The distribution of the contact resistance is assumed as constant. The simulation model is not able to describe deformations but current densities and heat development in the joint plane.

$$\mathrm{ECR}(T,P) = 3d\left(\frac{\sigma_S(T)}{P}\right)^K \left(\frac{\rho_{R1}(T) + \rho_{R2}(T)}{2}\right) \quad (1)$$

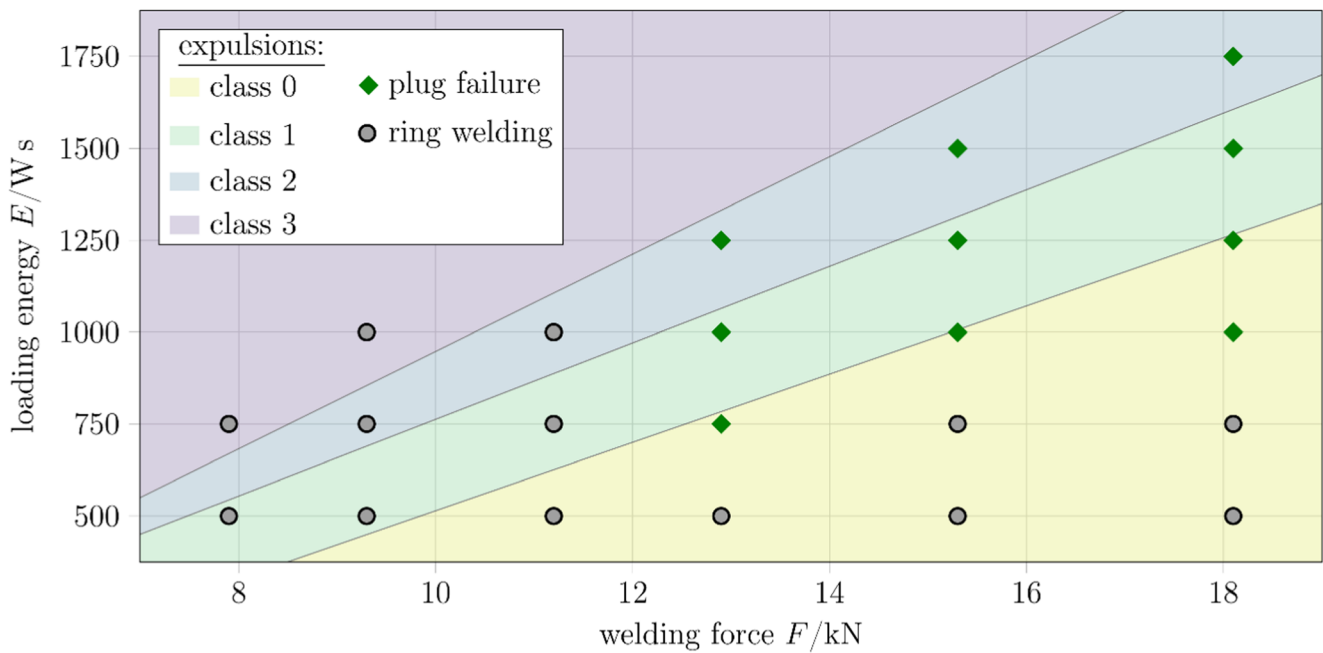| expulsion class	description	freeze image
0	no expulsions	
1	a few sparks/ expulsions	
2	more expulsions	
3	many and big expulsions	
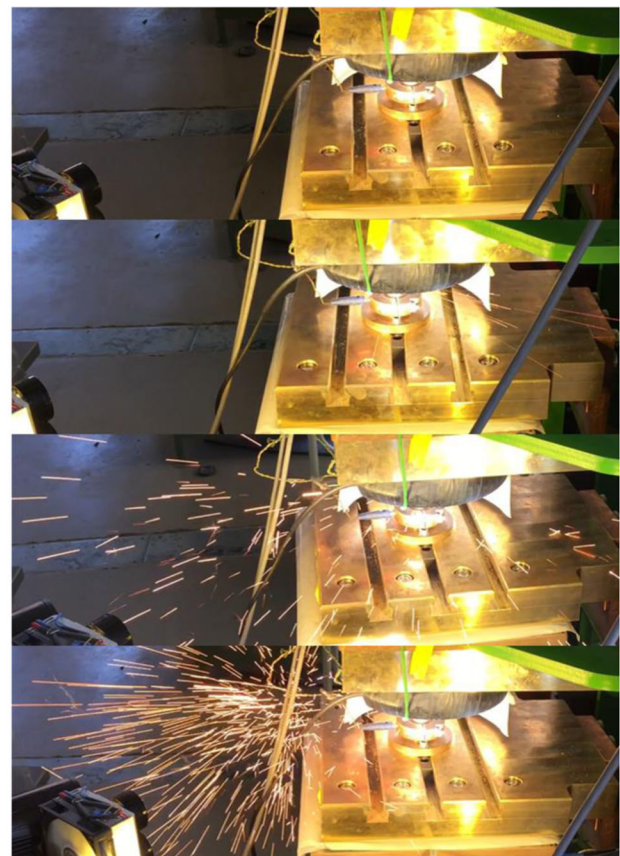
Fig. 3 Expulsion classes

Fig. 4 Weldability lobe of the single projection with the results of the chisel test and the classification of the expulsions

3 Discussion of the results

To analyse the welding results in further detail, cross sections were produced. Figure 6 shows a cross section of a single projection whose welding parameters caused ring welds ($F = 10$ kN, $E = 750$ Ws). The right part of the figure was taken after polishing but before etching, and the left part was taken after etching. On the polished part, there is a continuous transition between the edge area of the projection and the sheet metal, but in the middle of the projection, there is a lack of

fusion. On the etched part, no dilutions are visible. As a result, there is no weld nugget after the CD welding process. Simulation of the process can illustrate the temporal and local formation of the current density j. The current density got an inhomogeneous distribution (Fig. 7) even due to geometry, because the current is like a flow and the welding zone (in projection welding) like an orifice plate. The current/flow velocity is always higher at the edge of the projection area/orifice plate. The local heat flux density $\dot{q}$, which occurs due to the current pulse of the capacitor discharge and which causes the heating in
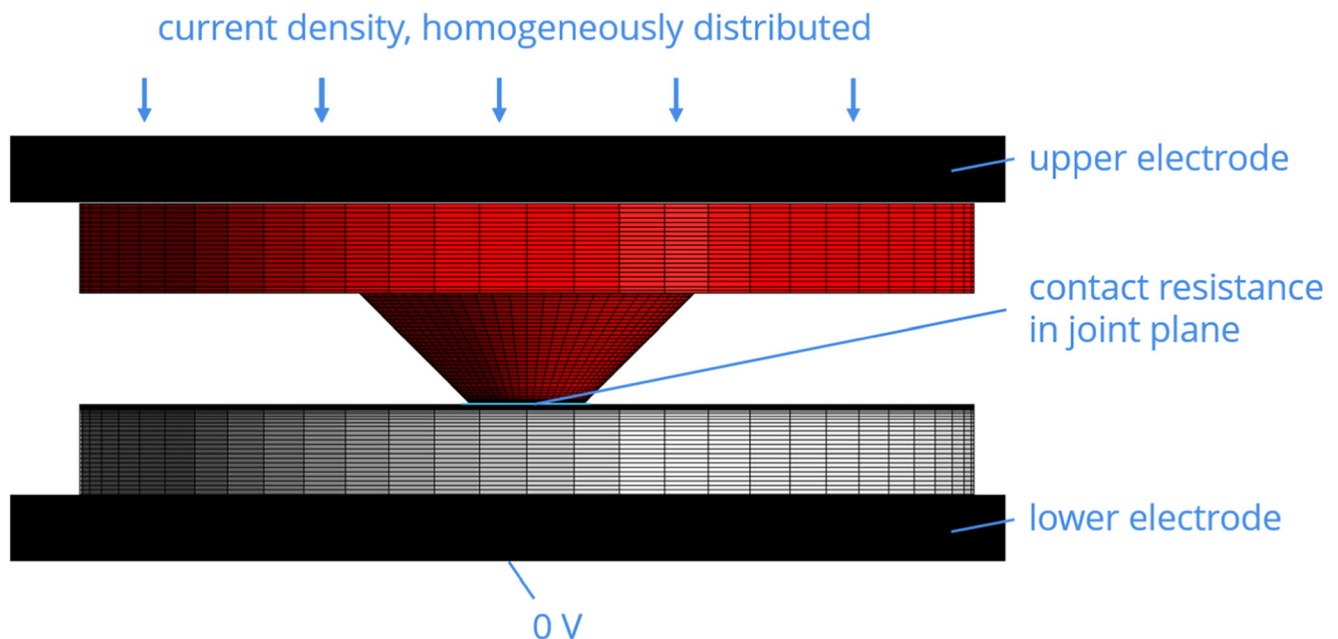

Fig. 5 Finite-volume-method simulation model of the singe projection
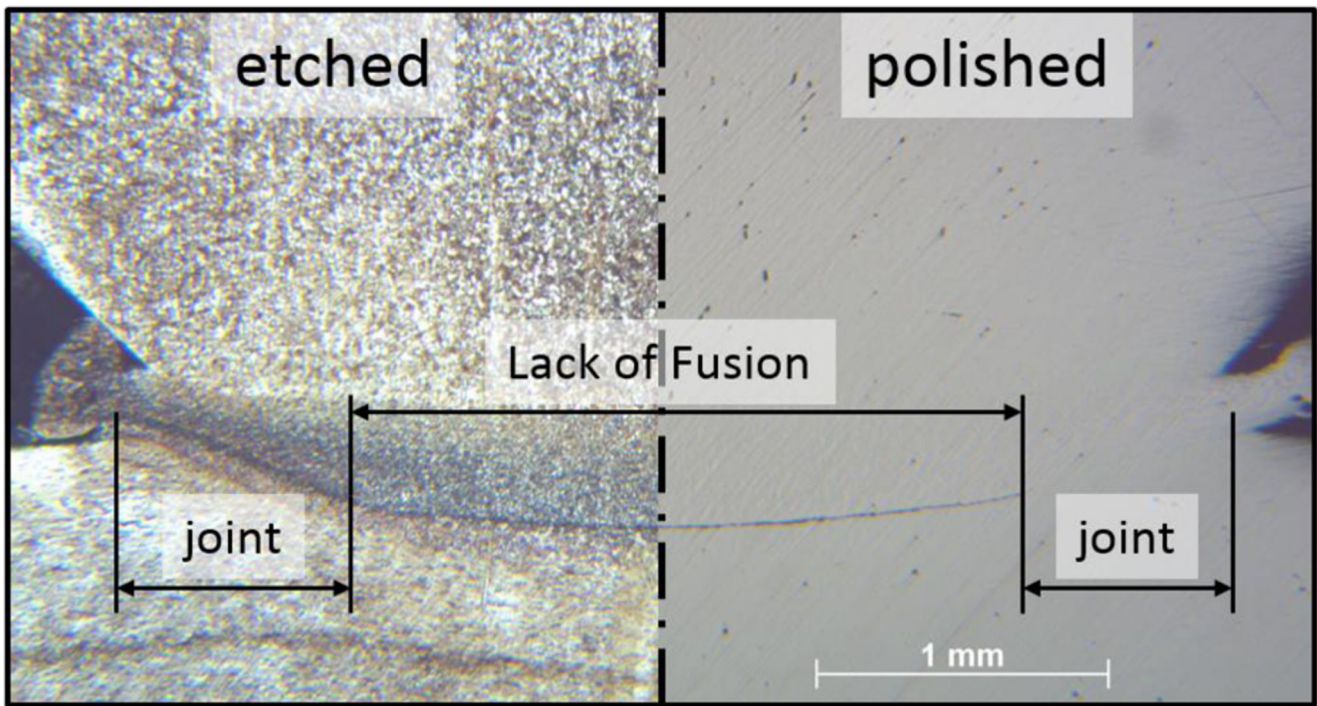
Fig. 6 Cross section of a welded single projection $F = 10$ kN, $E = 750$ Ws, left: after etching; right: before etching

the joint plane, is proportional to the square of the current density (Eq. 2, with resistance R of the contact and the material as constant of proportionality, current-carrying area A).

$$\dot{q} = \frac{\dot{Q}}{A} = j^2 \cdot R \tag{2}$$

Due to very high currents and current gradients, the heating rate is also very high. The local heat, which occurs due to high local current density, can barely conduct to the surrounding areas, caused by short welding time. As a result, there is a high difference in temperature between the edge area and the inner part of the joint plane. The simulation shows a temperature
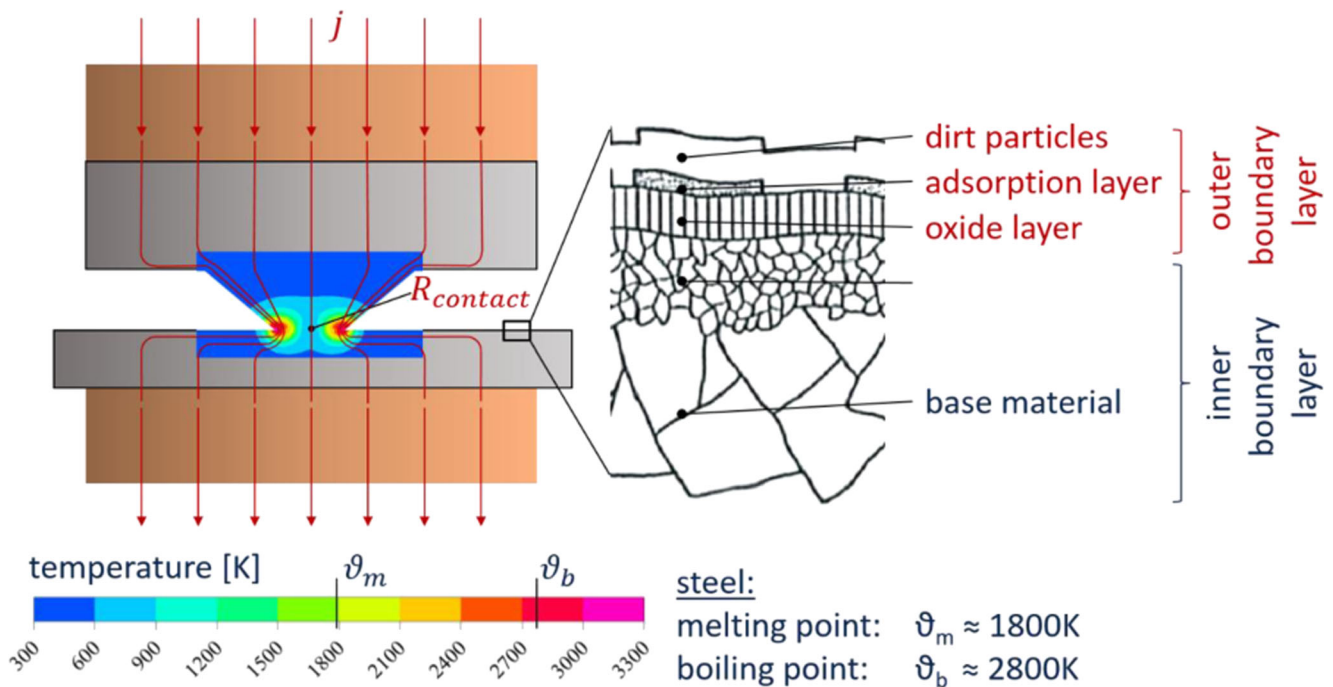

Fig. 7 Current density distribution and heating in the single projection; layers of a technical surface [19, 20]

higher than the boiling point of steel at the edge of the projection while the inner material of the joint plane is not molten yet. The metal vaporisation starts at the outer edge of the joint plane. During vaporisation, iron expands by about 33,000 times (estimated number, based on the volume of the vapour at boiling temperature and the volume of the solid state at room temperature). As a result, the metal vapour is massively accelerated. Disturbing layers (outer boundary layer, compare Fig. 7), which prevent formation of the joint, are removed, because the metal vaporises right under the oxide layers. The vapour takes along the oxide layers during the expansion. New oxide layers cannot emerge because of the chemical reductive behaviour of the hot metal vapour. Existing molten metal is also taken away. The joint is formed by pressing the activated surfaces together by the electrode force. The atoms of the joining partners get closer than the lattice constant of the unit cell (a few 10^{-11} m) and this results in a material joint [21].

There are always sudden micro-expulsions right before the current peak (Fig. 8). This type of expulsion is only visible in magnified high-speed-recordings. They occur even at expulsion class 0 without any macroscopically visible expulsions. The speed of these microscopic expulsions can be estimated up to 50 m/s (180 km/h) based on the distance the glowing particles pass within two pictures and the frames per second. This high speed can only be reached by metal vaporisation together with a huge expansion of the vapour. The micro-expulsions are regarded as evidence for metal vaporisation.

Furthermore, during CD welding high power is transformed (Fig. 8). With the power and the area of the joint plane, an average (related to the area of the welding zone A) power density can be calculated. The following calculation applies to the example in the moment of the power peak $\hat{P}$:

$$\dot{q} = \frac{P}{A} \approx 3 \cdot 10^6 \, \frac{\text{W}}{\text{cm}^2} \tag{3}$$

The estimated average power density $\hat{\dot{q}}$ causes the formation of a keyhole (caused by metal vaporisation) during laser beam welding [7]. In this calculation, the described inhomogeneous distribution of current density (Fig. 7) is ignored. The occurrence of metal vaporisation is proven by the simulation, the high-speed recordings and the measurement of the peak power.

The high current density in the edge area explains ring welds (Figs. 6 and 7). Plug failures indicate complete welded joint planes, but cross sections of chisel-tested welds (with plug failures as the result) show material joints only in the edge area of the projection, as well as ring welds (Fig. 10, right). Therefore, the maximum shear stress of the sheet metal was reached before the maximum normal tensile stress in the weld was reached during the chisel test. Nevertheless, it is possible to produce complete welded joint planes according to previous investigations [10].

Two hypotheses for the growth of the joined zone are formulated. The first hypothesis relates to the growth of the weld to the middle of the joint plane. The heat conduction is minimally conducive to heat the non-activated areas, because of the very short welding times. At the edge of the projection, metal vapour leaks under atmospheric pressure whereby the electrical conductive contact area decreases, as the metal vapour has very low electric conductivity [22]. The current flows through the progressively reduced area. There is always a higher current density at the edge of the contact area followed by metal vaporisation and activation of the surface. Therefore, the activation of the surface always starts at the edge and moves to the centre of the projection. This stops when the welding force decreases and the follow-up mechanism accelerates due to the ohmic heating of the joining partners linked with softening and material loss caused by vaporisation. The follow-up motion rebuilds the welding force. Then the activated areas are pressed together while molten material is pushed out of the joint plane. A material joint occurs, the contact resistance is eliminated, the current decreases steadily and therefore the current density decreases, too. The assumed process is illustrated in Fig. 9.
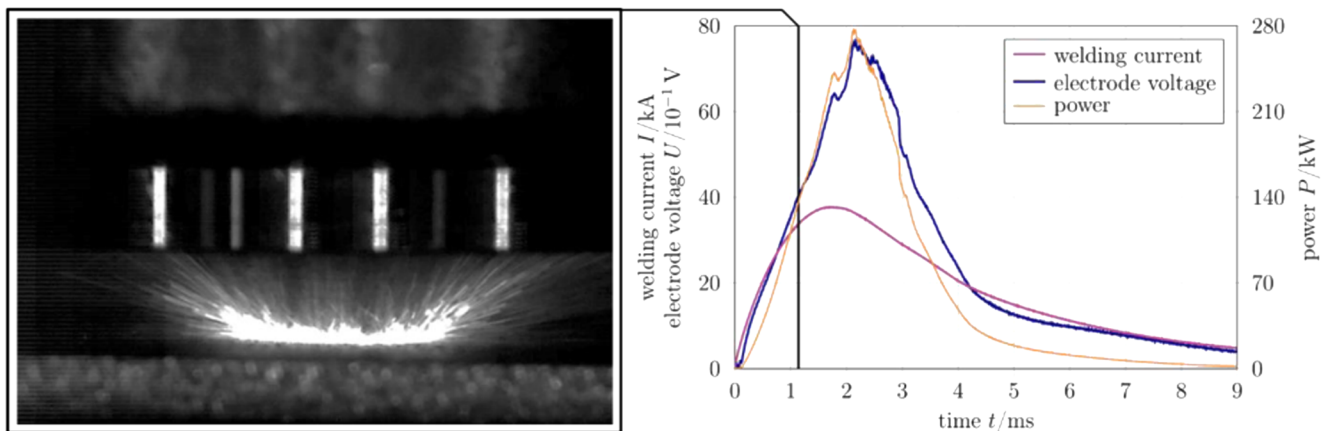
Fig. 8 Example of a welding with $E = 1000$ Ws and $F = 13.2$ kN, left: high-speed-recording at the signed time with micro-expulsions; right: parameter course
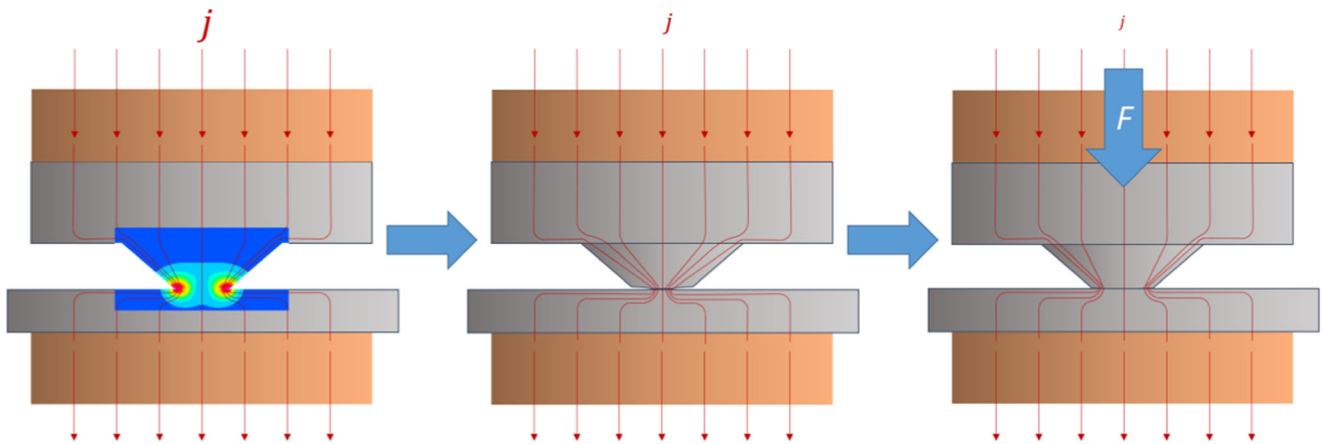
Fig. 9 Left: heating due to very high current density leads to metal vaporisation, starting shortly before the current peak is reached; middle: Area with metal vapour cannot conduct the current, current flows more to the middle of the joint plane, current decreases, depending on the heating more metal vaporisation occurs, electrode force decreases; right: follow-up mechanism accelerates and pushes joining partners together, current and current density decreases, no more metal vaporisation occurs

The bigger the difference between welding force (the preload force in the springs of the follow-up mechanism) and electrode force (the force which can be transmitted by the joint area) the bigger the acceleration of the follow-up mechanism is. The metal vaporisation achieves more progress at greater current gradients, as the peak current is higher in the same or shorter time. Without changes at the machine, the current gradient is higher—connected with higher peak currents in the same time by using more loading energy [23].

Accordingly, ring welds occur, when the metal vaporisation does not move to the centre of the joint plane and only the edge area is activated. Plug failures are formed, as soon as the area of the joint is big enough and the strength of the joint is higher than the maximum shear stress of the sheet metal material. In order to provide evidence for this, the average width of the annulus is assessed at the chisel-tested welds which are welded with F = 13,2kN and E = 500Ws/750Ws/1000Ws/1250Ws. The broken ring weld is used for measurement (the annulus is measured at two spots, Fig. 10). The cross sections of the plug failures are used in order to assess the annulus of the material joint (Fig. 10). The results are shown in Fig. 11. The higher the loading energy, the bigger the width of the annulus is, but measurement of the diameter of the lack of fusion shows only a small reduction in this investigation. Obviously, the ring-shaped weld grows more outwards than to the middle of the joint plane.

The second hypothesis relates to the outward growth. When the electrodes accelerate and push together the activated surfaces, molten material is pushed out of the joining zone. Material, which is soften, is displaced plastically to the outside of the welding zone. Oxide layers are displaced out of the joining zone, too, during this plastic displacement. This process is comparable with friction welding. The greater the energy converted in the joining zone, the more material is softened and plastically deformed. Furthermore, the more material is softened and plastically deformed, the closer the weld parts
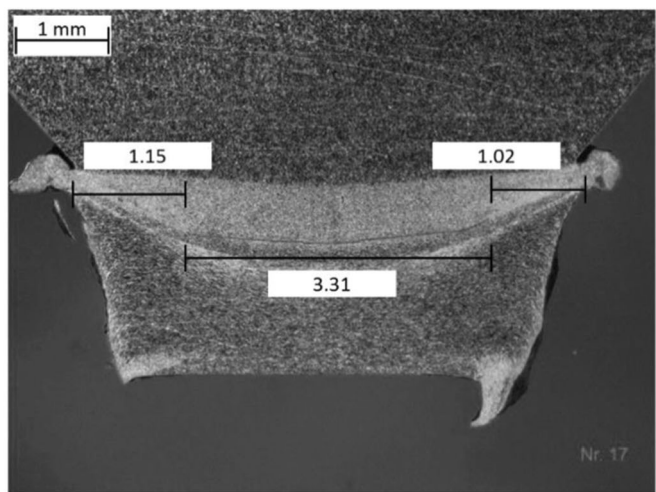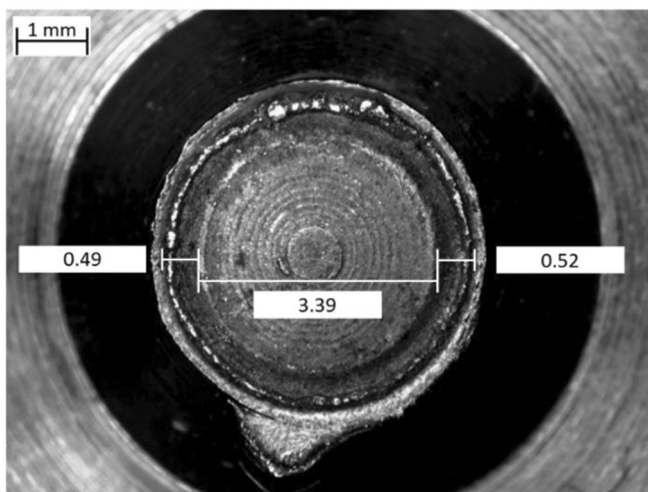
Fig. 10 Measuring method of the ring width at ring welds and plug failures
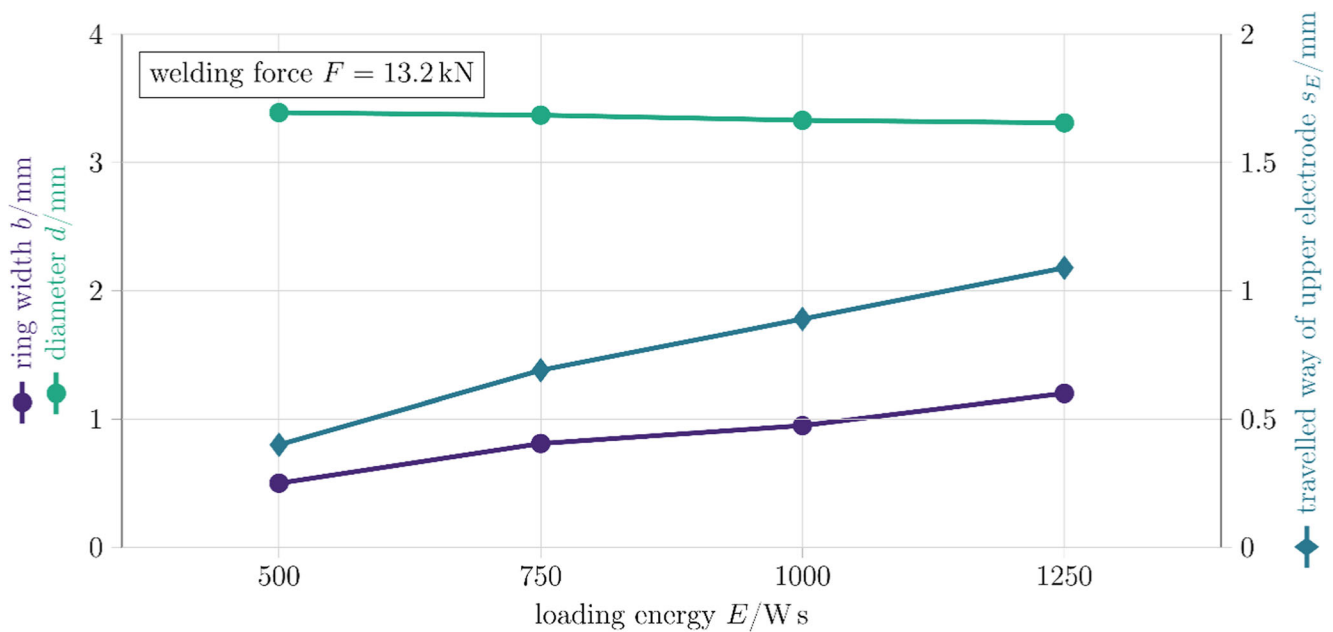
Fig. 11 Ring width and diameter of lack of fusion depending on loading energy at constant welding force F = 13.2 kN.

are pushed together. The difference of the measured distance between the upper and the lower electrode before and after welding (travelled way of upper electrode) proves this process (Fig. 11). The ring width also grows because of the projection geometry, i.e. the angle of 90 degrees. The closer the weld parts are pushed together, the bigger the welding zone gets.

4 Conclusion and outlook

This paper examines the formation of joints at capacitor discharge welding. It provides evidence for metal vaporisation due to high current density at the edge area of the geometry of welding projections. Furthermore, the paper describes two hypotheses for the process of the growth of the welding zone. At first, the increased current density moves to the centre of the projection as the electric conductivity of metal vapour is very low. Therefore, the metal vaporisation can activate the whole joint plane, starting at the edge of the projection. The force of the electrodes presses the activated surfaces together. Consequently, the joint occurs. Secondly, the softened material is displaced plastically, and the weld grows comparable with the process of friction welding (solid state welding). These hypotheses need further investigations.

In cross sections, there are no weld nuggets, as the joints are formed without dilution of molten material, which is taken out of the joint plane due to accelerated metal vapour or is extruded by the follow-up motion of the electrodes. As a result, weld nuggets cannot be an acceptance criterion for the destructive-testing with cross sections. Destructive testing with a quantifiable result, e.g. normal tensile test, is more useful. Furthermore, micro-expulsions have to be accepted,

since they are linked to the metal vaporisation. Expulsions can be tolerated with suitable constructive measures (e.g. a barrier that protects critical parts from expulsions). An expulsion-free (macroscopic) CD process can be done with variations of the process [23]. In order to deepen the knowledge of CDW, the simulation model will be extended by the deformation of the joint plane during welding. Therewith, findings of appropriate projection geometry and temperature distributions are useful, in order to retain CDW's status as an efficient and reliable welding process while expanding its field of application.

References

1. Piersig W (2010) Geschichtlicher Überblick zur Entwicklung der Metallbearbeitung: Beitrag zur Technikgeschichte (8). GRIN Verlag GmbH, München
2. Normenausschuss Schweißtechnik (NAS) im DIN (2008) Schweißen und verwandte Prozesse - Begriffe - Teil 100: Metallschweißprozesse mit Ergänzung zu DIN EN 14610: 2005(DIN 1910–100:2008–02)
3. Normenausschuss Schweißtechnik (NAS) im DIN (2005) Schweißen und verwandte Prozesse - Begriffe für

Metallschweißprozesse; Dreisprachige Fassung EN 14610: 2004(DIN EN 14610:2005–02)

4. Deutscher Verband für Schweißen und verwandte Verfahren e.V. (2010) Steuerungen und Leistungsteile für das Widerstandsschweißen (DVS 2904)

5. Deutscher Verband für Schweißen und verwandte Verfahren e.V. (2016) Kondensatorentladungsschweißen – Grundlagen, Verfahren und Technik (DVS 2911)

6. Früngel FB (1960) Das Kondensator-Impulsschweißen: Wirkungsweise und Vorteile des Verfahrens - Physikalische Grundlagen - Durchführung des Verfahrens - Verwendete Schweißelektroden - Maschinelle Ausrüstung. Schweissen und Schneiden 12(1):14–18

7. Dilthey U (2006) Schweißtechnische Fertigungsverfahren 1: Schweiß- und Schneidtechnologien, 3., bearbeitete Auflage. VDI-Buch. Springer-Verlag, Berlin

8. Cramer H (2007) Untersuchungen zum Anschweißen von Widerstandsschweißmuttern an Bleche aus höher- bis höchstfesten Werkstoffen: AiF-Nr. 14.435N DVS-Nr. 04.039, München

9. Cramer H (2003) Widerstandsschweißen von höherkohlenstoffhaltigen Stählen mit sehr kurzer Wärmeeinbringung: AiF-Nr. 2037/00 DVS-Nr. 4.027, München

10. Zschetzsche J, Füssel U, Hertel M et al (2016) Kurzzeitschweißen mit hoher Wärmestromdichte. In: Widerstandsschweißen: Vorträge der gleichnamigen 23. Sondertagung in Duisburg am 29. und 30. Juni 2016, Als Manuskript gedruckt, vol 326. DVS Media, Düsseldorf, pp 223–229

11. Normenausschuss Schweißtechnik (NAS) im DIN (1996) Buckel für das Buckelschweißen von Stahlblechen. Langbuckel und Ringbuckel (DIN 8519)

12. Dilthey U, Dickersbach J, Bohlmann H-C (1998) Optimisation of the projection geometry for welding with capacitor pulsed current. Weld Cut 50(1):E2–E5

13. Cramer H (2010) Optimierung der Geometrie geprägter Buckel für das Widerstandsbuckelschweißen an höher- bis höchstfesten Stahlwerkstoffen: AiF-Nr. 15.534N DVS-Nr. 04.045, München

14. Normenausschuss Eisen und Stahl (FES) im DIN Warmgewalzte Erzeugnisse aus Baustählen - Teil 2: Technische Lieferbedingungen für unlegierte Baustähle(EN 10025–2)

15. Salzgitter Flachstahl GmbH (05/14) 22MnB5 - Kaltband: Vergütungsstahl, borlegiert. https://www.salzgitter-flachstahl.de/fileadmin/mediadb/szfg/informationsmaterial/produktinformationen/kaltgewalztes_feinblech/deu/22mnb5.pdf. Accessed 19 Mar 2019

16. Ketzel M-M, Zschetzsche J, Füssel U (2017) Elimination of voltage measuring errors as a consequence of high variable currents in resistance welding. Weld Cut 16(3):164–168

17. Normenausschuss Schweißtechnik (NAS) im DIN (2015) Widerstandsschweißen – Prüfung von Schweißverbindungen – Schäl- und Meißelprüfung von Widerstandspunkt- und Buckelschweißverbindungen(DIN EN ISO 10447:2007–09)

18. Wan Z, Wang H-P, Wang M, Carlson BE, Sigler DR (2016) Numerical simulation of resistance spot welding of Al to zinc-coated steel with improved representation of contact interactions. Int J Heat Mass Transf 101:749–763. https://doi.org/10.1016/j.ijheatmasstransfer.2016.05.023

19. Pejko M (2010) Fügbarkeitsbetrachtungen von Press-Presslöt-Verbindungen. Zugl.: Dresden, Techn. Univ., Diss., 2009. Dresdner fügetechnische Berichte, vol 19. TUD Press Verl. der Wiss, Dresden

20. Fischer U (2008) Tabellenbuch Metall, 44., neu bearb. Aufl. Europa-Fachbuchreihe für Metallberufe. Verl. Europa-Lehrmittel, Haan-Gruiten

21. Ruge J, Wohlfahrt H (2007) Technologie der Werkstoffe: Herstellung Verarbeitung Einsatz, 8., überarbeitete und erweiterte Auflage. Friedr. Vieweg & Sohn Verlag | GWV Fachverlage GmbH Wiesbaden, Wiesbaden

22. Braunbek W (1935) Über die elektrische Leitfähigkeit komprimierter Metalldämpfe. Z Physik (Zeitschrift für Physik) 97(7–8):482–495. https://doi.org/10.1007/BF01330917

23. Rusch H-J (2016) Neue Möglichkeiten der Prozessgestaltung beim KE-Schweißen. In: Widerstandsschweißen: Vorträge der gleichnamigen 23. Sondertagung in Duisburg am 29. und 30. Juni 2016, Als Manuskript gedruckt. DVS Media, Düsseldorf, pp 201–210